



1 **Climatology and annual cycle of global ocean dissolved oxygen represented by multiple**
2 **observational gridded products**

3 Juan Du¹, Lijing Cheng², Takamitsu Ito³, Hernan E. Garcia⁴, Zhankun Wang⁵, Jonathan D.
4 Sharp⁶, Christopher J. Roach⁷, Shoshiro Minobe⁸, Yuntao Zhou⁹, Bin Lu¹⁰, Gian Giacomo
5 Navarra¹¹, Seth M Bushinsky¹²

6
7 ¹ International Center for Climate and Environment Sciences, Institute of Atmospheric
8 Physics, Chinese Academy of Sciences, Beijing, China.

9 ² State Key Laboratory of Earth System Numerical Modeling and Application, Institute of
10 Atmospheric Physics, Chinese Academy of Sciences, Beijing, China.

11 ³ School of Earth and Atmospheric Sciences, Georgia Institute of Technology, Atlanta,
12 Georgia, USA.

13 ⁴ NOAA, National Centers for Environmental Information, Silver Spring, Maryland, USA.

14 ⁵ Cooperative Institute for Climate, Ocean, and Ecosystem Studies, University of Washington,
15 Seattle, Washington, USA.

16 ⁶ Pacific Marine Environmental Laboratory, National Oceanic and Atmospheric
17 Administration, Seattle, Washington, USA.

18 ⁷ Institute for Marine and Antarctic Studies, University of Tasmania, Hobart, Australia.

19 ⁸ Department of Earth and Planetary Sciences, Faculty of Science, Hokkaido University,
20 Sapporo, Japan.

21 ⁹ School of Oceanography, Shanghai Jiao Tong University, Shanghai, China.

22 ¹⁰ School of Information Science and Electronic Engineering, Shanghai Jiao Tong University,
23 Shanghai, China.

24 ¹¹ Department of Geosciences, Princeton University, Princeton, New Jersey, USA.

25 ¹² Department of Oceanography, School of Ocean and Earth Science and Technology,
26 University of Hawaii at Manoa, Honolulu, Hawaii, USA.

27
28 **Corresponding author:** Juan Du (dujuan10@mail.iap.ac.cn)

29

30 **Abstract:**

31 Ocean dissolved oxygen (O₂) is an essential climate variable crucial for sustaining the marine
32 life; thus, changes of O₂ at various spatiotemporal scales should be quantified and
33 understood. Here, we study the climatology and annual cycle of O₂ at regional to global
34 scales using eight available gridded observational products. These datasets are generated by
35 different groups using different primary data selection, quality control, bias correction and
36 interpolation methods including statistical and machine-learning based mapping methods. A
37 common set of metrics was collaboratively developed by the community of Gridded
38 Observational Dataset Intercomparison Project-Dissolved Oxygen (GODIP-DO) to facilitate
39 the inter-comparison, which allows assessing the robustness of the uncertainties through the
40 spread of the products. Global mean O₂ profiles are consistent among all products ($\pm 3 \mu\text{mol}$
41 kg^{-1}), with the well-established decrease from high surface values to a minimum ~ 1000
42 meters, and subsequent increase to higher O₂ at depth, although local differences could reach



43 $\pm 25 \mu\text{mol kg}^{-1}$ (0-1000 m). The hemispheric O_2 annual cycle correlates strongly with ocean
44 temperature changes, suggesting the key driver of temperature for the O_2 annual cycle.
45 However, there is substantial variation in the global mean 0-100 m O_2 annual cycle, the
46 magnitude ranges from -1 to $0.8 \mu\text{mol kg}^{-1}$, with a standard deviation of the datasets of ~ 0.3
47 $\mu\text{mol kg}^{-1}$. Average oxygen minimum zones (OMZ) volume among the products is $80.92 \times$
48 10^6 km^3 ($\pm 1.95 \%$) for a $60 \mu\text{mol kg}^{-1}$ threshold and $152.00 \times 10^6 \text{ km}^3$ ($\pm 1.72 \%$) for a 90
49 $\mu\text{mol kg}^{-1}$ threshold. Our results serve as a starting point for resolving the uncertainty budget
50 of the ocean O_2 changes.

51

52 **1 Introduction**

53 Anthropogenic climate change drives ocean warming, increases stratification, and alters
54 ocean circulation (Bindoff et al. 2019). These changes lead to the loss of ocean dissolved
55 oxygen (O_2), namely deoxygenation, because of the changes in the O_2 solubility, ventilation,
56 and deep ocean respiration (Keeling et al., 2010; Schmidtko et al., 2017; Breitburg et al.,
57 2018; Oschlies et al., 2018; Garcia-Soto et al., 2021). Deoxygenation occurred in most open
58 ocean regions during the mid-20th to early 21st centuries, influencing marine ecosystems
59 through resulting biogeochemical feedbacks such as ocean productivity, nutrient cycling,
60 carbon cycling, marine habitat, etc (Levin, 2018; Bindoff et al., 2019). Given its importance,
61 studying O_2 changes at various spatiotemporal scales becomes critical.

62 Observations and model simulations document a robust decline of the global O_2
63 inventory, which is a grand challenge for the accurate assessment of deoxygenation (Ito et al.,
64 2017; Schmidtko et al., 2017; Breitburg et al., 2018). For trends, current assessments such as
65 the IPCC Special Report on the Ocean and Cryosphere in a Changing Climate (SROCC)
66 indicates that the open ocean is losing O_2 overall with a decadal variability of 0.3% – 2%
67 since the 1960s over all ocean depths and of 0.5% – 3.3% between 1970 and 2010 from the
68 ocean surface to 1000 m, with an expansion of oxygen minimum zones (OMZ) by 3 – 8%
69 (Bindoff et al., 2019; Gulev et al., 2021; Zhou et al., 2022). These studies reveal substantial
70 uncertainty in quantifying the open ocean O_2 trends, however, there is no dedicated study
71 assessing the available products on O_2 climatology and its annual cycle, which is the key
72 focus of the present study.

73 The differences among different O_2 products may arise from the instruments/platforms
74 used to obtain O_2 profiles and the data processing techniques including quality control
75 processes; bias correction approaches; vertical interpolation methods; mapping methods



76 (horizontal interpolation); land-ocean masks and so on. Since the late 19th century,
77 oceanographers have measured ocean O₂ using many instruments. The very first instrument
78 includes the chemical titration method developed by Winkler (Ocean Station Data, OSD),
79 which restricted the O₂ observations derived from water samples to several depth levels.
80 Electrochemical and optical sensors for measuring O₂ became prevalent in the 1960s-70s and
81 are now widely used to make continuous measurements on platforms such as the CTD
82 (Conductivity-Temperature-Depth) profilers. Biogeochemical Argo profiling floats (BGC-
83 Argo) have provided increasing ocean O₂ observation profiles since the early 2000s, and
84 underwater gliders (GLD) and moorings are especially useful for regional oceanography
85 (Gregoire et al., 2021; Gourteski et al., 2024).

86 With the ocean O₂ observations collected using different observing systems, there have
87 been several quality controlled global ocean O₂ observation datasets from different research
88 organizations/groups such as the National Centers for Environmental Information (NCEI) of
89 the National Oceanic and Atmospheric Administration (NOAA) (Garcia et al., 2024; Garcia
90 et al., 2018; Boyer et al., 2018), Shanghai Jiao Tong University (SJTU, Zhou et al. 2022) and
91 the Institute of Atmospheric Physics (IAP) Chinese Academy of Sciences (Gourteski et al.,
92 2024). These quality controlled observations are then used to construct gridded O₂ data
93 products by filling data gaps with a mapping method where direct observations were not
94 available. The available mapping methods include objective analysis (Garcia et al., 2024),
95 ensemble optimal interpolation with dynamic ensemble (EnOI-DE, Cheng et al., 2024; Cheng
96 et al., 2017, Cheng and Zhu, 2016), Data Interpolating Variational Analysis (DIVA; Roach
97 and Bindoff, 2023), machine learning techniques (Sharp et al., 2023; Ito et al., 2024; Huang
98 et al., 2023; Liu et al., 2025), and geostatistical regression (Zhou et al., 2022).

99 All the previously mentioned instrumental data have measurement errors and biases,
100 and the data processing techniques are imperfect, leading to uncertainty in representing the
101 O₂ climatological mean state and its annual variation. A systematic multi-product
102 intercomparison at regional to global scales could serve as the primary tool to assess the
103 robustness of our observational understanding and to quantify the overall uncertainty inherent
104 in current climatological representations. Our comprehensive approach to assess uncertainties
105 including all factors is different from the recent single-factor assessment of Ito et al. (2025)
106 who focused solely on mapping methods. In particular, we employed eight ocean O₂
107 climatology products, covering statistical and machine-learning based mapping methods
108 whereas Ito et al. (2025) included statistical mapping methods only. Our analysis includes the
109 gridded O₂ dataset from the Institute of Atmospheric Physics (hereafter, IAP; Gourteski et al.,



110 2024), World Ocean Atlas 2023 (hereafter, WOA23; Garcia et al., 2024) and World Ocean
111 Atlas 2018 (hereafter, WOA18; Garcia et al. 2018, Boyer et al., 2018) by NCEI, a machine
112 learning-based data product by Sharp et al. (Gridded Ocean Biogeochemistry from Artificial
113 Intelligence, hereafter, GOBAl; Sharp et al. 2023), two data products based on DIVA
114 by Roach and Bindoff (hereafter, RB; Roach and Bindoff, 2023) and Global Ocean Data
115 Analysis Project (hereafter, GLODAP; Lauvset et al., 2016), a geostatistical gridded O₂
116 dataset from Shanghai Jiao Tong University (hereafter, SJTU; Zhou et al., 2022), and a
117 machine learning-based data product (hereafter, Jingwei; Lu et al., 2024).

118 The rest of the paper is organized as follows. The gridded datasets and methods
119 employed in the study are presented in Section 2. In Section 3, the results of depicting the
120 characteristics and assessing the uncertainties of O₂ climatology and annual cycle for
121 different products are introduced. The analysis related to OMZ distribution is also presented
122 in Section 3. The results of the study are summarized and discussed in Section 4.

123

124 **2 Datasets description**

125 We used eight O₂ gridded products (IAP, WOA23, WOA18, GOBAl, RB, GLODAP,
126 SJTU, and Jingwei) which are different in many aspects including the instruments to get raw
127 O₂ profiles and also the data processing techniques, such as quality control and bias
128 correction approaches, vertical interpolation methods, mapping methods, land-ocean masks
129 and so on (**Table 1**).

130 The observations used by IAP, WOA23, WOA18, RB, SJTU and Jingwei are mainly
131 from WOD (World Ocean Database, Boyer et al., 2018; Mishonov et al., 2024) and BGC-
132 Argo. Observations from GLODAP are also used in GOBAl product. The IAP, WOA23,
133 WOA18 and GOBAl datasets include monthly climatology, and the remaining four data
134 products only provide the annual mean climatology. So, analyses related to the annual
135 variation of the global ocean O₂ and the annual cycle are restricted to the four datasets with
136 monthly climatology. The gridded data products of IAP, WOA23, WOA18, RB, GLODAP,
137 and Jingwei reach the ocean bottom of about 5500 m/6000 m. GOBAl, and SJTU only cover
138 the top 2000m. The horizontal resolution of the data product of RB and SJTU is 0.5° × 0.5°
139 and 2° × 2°, respectively, and all the other six products are at a resolution of 1° × 1°. The
140 horizontal space coverages of all the datasets are also slightly different. The space coverage
141 of the GOBAl data is limited by the distribution of the temperature and salinity data product
142 on which it is based, so GOBAl only covers 64.5° S-79.5° N of the open ocean (O₂ in the
143 coastal regions and oceans with complex topography are not reconstructed). The mapping



144 method for WOA18 and WOA23 is based on objective analysis (OA) and that for IAP is the
 145 ensemble optimal interpolation with dynamic-ensemble (EnOI-DE). GLODAP and RB both
 146 adopt the Data-Interpolating Variational Analysis (DIVA) method to generate gap-filled
 147 fields. SITU develops the geostatistical regression (GR) interpolation method. The feed-
 148 forward neural network and the spatio-temporal graph hypernetwork are used for the machine
 149 learning (ML) process of the GOBAI and Jingwei data products, respectively (**Table 1**).

150

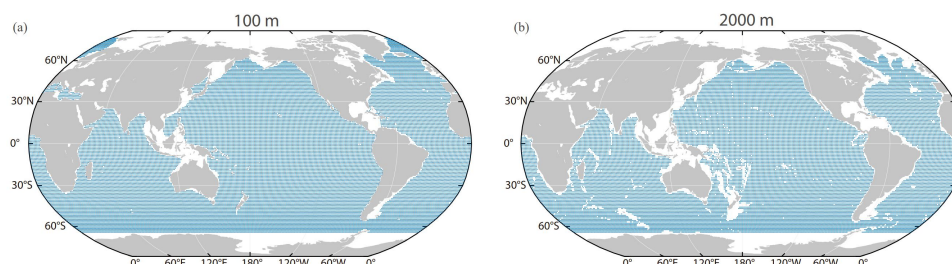
151 **Table 1** Global ocean O₂ gridded datasets employed in the comprehensive inter-comparison
 152 of the climatology.

O ₂ datasets	mapping	quality control	time period	resolution	depth/ layers	observations
IAP Gourteski et al., 2024	EnOI-DE	IAP	1960-2022	1° × 1°	6000 m/119	OSD, CTD, Argo
WOA23 Garcia et al., 2024	OA	NCEI	1965-2022	1° × 1°	5500 m/102	OSD, CTD, Argo
WOA18 Boyer et al., 2018	OA	NCEI	1960-2017	1° × 1°	5500 m/102	OSD
GOBAI Sharp et al., 2023	ML	GLODAP, Argo	2004-2024	1° × 1°	1975 m/58	OSD, Argo
RB Roach and Bindoff, 2023	DIVA	NCEI	1960-2017	0.5° × 0.5°	6100 m/108	OSD, CTD
GLODAPv2 Lauvset et al., 2016	DIVA	GLODAP	1972-2013	1° × 1°	5500 m/33	OSD, WOCE, CLIVAR/GO-SHIP
SJTU Zhou et al., 2022	GR	NCEI, SJTU	1960-2019	2° × 2°	2000 m/61	OSD, CTD, GLD, Argo
Jingwei Lu et al., 2024	ML	NCEI	1960-2023	1° × 1°	5500 m/33	OSD, CTD, Argo

153



154 This study used a common ocean mask, which is defined as ocean grid points with all
155 data products available. The common land-ocean masks for the layers of 100 m and 2000 m
156 are presented in **Fig. 1** and the common masks for the other layers (1000 m, 3000 m, 4000 m
157 and 5000 m) are available in **Fig. S1**. This will be a uniform comparison and remove the
158 impacts of different data coverage on the results. The datasets of RB and SJTU were
159 interpolated to a common $1^\circ \times 1^\circ$ resolution as all the other datasets to facilitate the
160 comparison, but the interpolation has a negligible impact on the results presented in this
161 work.



162

163 **Figure 1** Grid point distribution of the common land-ocean mask for the layers of 100 m (a)
164 and 2000 m (b).
165

166 3 Results

167 3.1 Global mean O_2

168 The global area-weighted mean O_2 profile is first presented in **Fig. 2a**, showing a well-
169 established vertical structure and a good consistency among all products. O_2 is higher near
170 the surface than in the deeper ocean because of the gas exchange with the atmosphere and
171 photosynthesis. The O_2 reaches the lowest value at ~ 1000 m because of the respiration and
172 limited O_2 supply from the surface. The O_2 increases from ~ 1000 m to the deep ocean (~ 5000
173 m) because of the weaker respiration and the intermediate, deep and bottom water formation
174 that supplies higher O_2 water into the deep layers, where cold, dense surface water sinks, and
175 is then distributed globally by deep ocean currents, slowly losing O_2 along its centuries-long
176 journey (Musan et al., 2023).

177 To better quantify the differences among the datasets, we take the difference between all
178 seven other data products (WOA23, WOA18, GOBAl, RB, GLODAP, SJTU, and Jingwei),
179 and IAP data (**Fig. 2b**). The differences are mostly within $\pm 3 \mu\text{mol kg}^{-1}$ among all the
180 datasets with a common land-ocean mask from ocean surface to 5500 m, except that the
181 differences for SJTU and Jingwei range between -6 and $5 \mu\text{mol kg}^{-1}$ for the upper 200 meters.



182 The differences are comparable to the magnitude of O₂ anomaly, whose semi-decadal median
183 is within $\pm 10 \mu\text{mol kg}^{-1}$ within major ocean basins (Schmidtko et al., 2017).

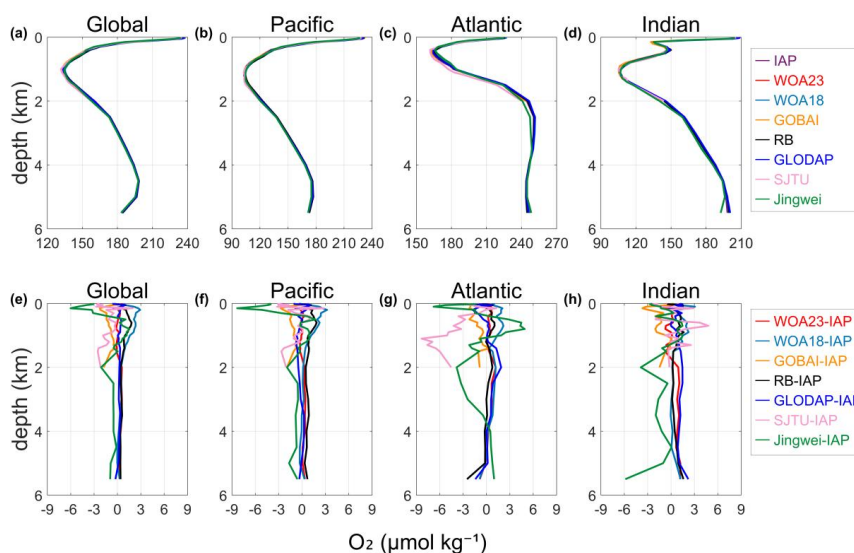
184 There is a negative offset between GOBAI and IAP ($\sim -2 \mu\text{mol kg}^{-1}$). The differences
185 between WOA18, RB and IAP are positive. One possible reason for these differences is that
186 different data products construct climatology using data from different time periods with
187 different resolutions. The SJTU climatology uses CTD, OSD, Argo, and additional GLD
188 data, then interpolate them at coarser 2° resolution. The GOBAI climatology is reflective of a
189 more recent period compared to the other datasets (2004-2024), which might at least partly
190 explain the negative difference between GOBAI and IAP (where data from 1960-2022 are
191 used). Because of the general deoxygenation trend, a “newer” climatology is expected to
192 show less global mean O₂ than an “older” climatology. IAP is close to WOA23 at the upper
193 2000 m within $1 \mu\text{mol kg}^{-1}$, which is reasonable because both IAP and WOA23 used bottle
194 (OSD), CTD and delayed-mode Argo data using the same 1° data resolution, and they have
195 similar time coverage of data used to generate climatology (IAP, 1960-2022 and WOA23,
196 1965-2022).

197 Below 2000 m, there is an offset between IAP and WOA23: WOA23 O₂ is 0.2-0.6 μmol
198 kg^{-1} higher than IAP. Possible explanations may be the differences in quality control and
199 mapping methods. Another possibility is the ‘jump’ around 2000 m of IAP minus WOA23. It
200 is common to have a discontinuity around 2000 m because of the big differences in data
201 amount and data distributions at upper and deeper layers (Observations are concentrated in
202 the upper ocean and most of the Argo data are in the upper 2000 m). Differences in infilling
203 the empty grid nodes during the mapping procedure may also play a significant role in deep
204 ocean layers where the number of observation data is severely limited. Results of applying
205 different mapping methods to the same in situ datasets suggest that mapping methods may
206 contribute to a difference of less than $\pm 1 \mu\text{mol kg}^{-1}$ for the 0-5500 m area-weighted averaged
207 O₂ (Ito et al., 2025). And using two different quality control processes and the same mapping
208 procedure yields a difference of only $\pm 0.5 \mu\text{mol kg}^{-1}$ (Ito et al., 2025).

209 The mean O₂ profiles and the differences between datasets for major ocean basins
210 (Pacific, Atlantic, Indian) are calculated separately and presented in **Fig. 2b-d** and **Fig. f-h**.
211 The differences are mostly within $\pm 4 \mu\text{mol kg}^{-1}$ among all the datasets for the Pacific and
212 Indian Ocean, except that the difference for Jingwei ranges between -8 and $2 \mu\text{mol kg}^{-1}$ for
213 the upper 200 meters in the Pacific Ocean (**Fig. 2f**). The mean O₂ profiles for the Atlantic
214 Ocean show more notable differences compared to other ocean basins (**Fig. 2c**), including



215 that the mean O_2 profile of SJTU data shows a difference of -10 to $-5 \mu\text{mol kg}^{-1}$ for the depth
 216 of 1000 - 2000 m, while the differences of all the other datasets are constrained to -5 to $5 \mu\text{mol}$
 217 kg^{-1} from ocean surface to the depth of 5500 m (**Fig. 2g**). For the Atlantic Ocean, the mean
 218 O_2 reached the minimum at the depth of ~ 500 m (**Fig. 2c**) which is much shallower than the
 219 O_2 minimum layers for the Pacific Ocean and Indian Ocean (~ 1000 m, **Fig. 2b, 2d**), possibly
 220 due to a combined effect of the formation, transport and mixing process of the North Atlantic
 221 Deep Water (NADW), the ventilation processes such as Atlantic Meridional Ocean
 222 Circulation (AMOC) and so on (Levin, 2018; Koelling et al., 2022; Musan et al., 2023; Ruhl
 223 et al., 2025).
 224



225
 226 **Figure 2** Area-weighted mean O_2 climatology (a-d) and difference (e-h) relative to the IAP
 227 for the Global, Pacific, Atlantic and Indian Ocean from ocean surface to 5500 m with a
 228 common ocean mask for different ocean basins in units of $\mu\text{mol kg}^{-1}$. The subplots for O_2
 229 climatology (a-d) use different scales.
 230

231 3.2 Zonal mean structure

232 The global zonal mean O_2 concentration of the eight datasets for the upper 1000 m
 233 shows consistency for the zonal structure (**Fig. 3a**). There is a minimum of mean O_2 levels
 234 around the tropical regions for all the datasets, associated with a shoaling of the tropical and
 235 subtropical thermocline depth (Deutsch et al., 2011) and the presence of the tropical upper
 236 ocean OMZ. The differences in the global zonal mean O_2 for the upper 1000 m between the

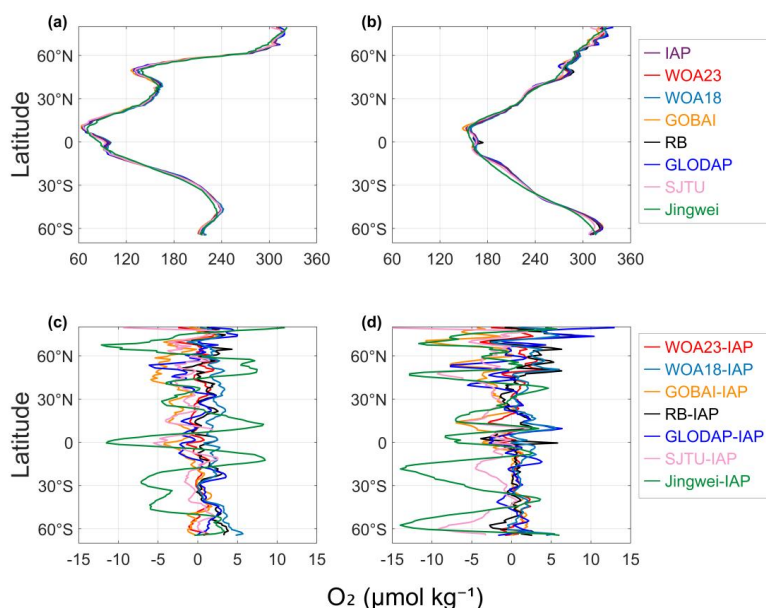


237 seven data products (WOA23, WOA18, GOBAI, RB, GLODAP, SJTU and Jingwei) and IAP
238 are shown in **Fig. 3b**). The differences in zonal mean 0-1000 m averaged O_2 are mostly
239 within $\sim 5 \mu\text{mol kg}^{-1}$. The zonal mean O_2 difference between IAP and WOA23 is the smallest,
240 which is generally within $\sim 1.5 \mu\text{mol kg}^{-1}$. The zonal mean of GOBAI is generally lower than
241 that of IAP, especially in the Northern Hemisphere, which may imply stronger deoxygenation
242 trends in the Northern Hemisphere, as the GOBAI climatology baseline is newer than that of
243 IAP. The zonal mean of the RB dataset is higher than that of IAP by $\sim 0.78 \mu\text{mol kg}^{-1}$ on
244 average, consistent with the positive offset shown in **Fig. 2**. Jingwei dataset has the strongest
245 differences from IAP and other products, showing a notable zonal fluctuation.

246 The results for the depth layers 0-600 m and 0-2000 m (**Fig. S2**) show similar variation
247 pattern to the depth layer 0-1000 m. The differences in the global zonal mean O_2 between
248 data products are mostly within $\sim 5 \mu\text{mol kg}^{-1}$ for 0-600 m and within $\sim 3 \mu\text{mol kg}^{-1}$ for 0-2000
249 m (**Fig. S2b, S2d**). For 0-600 m, the zonal mean O_2 difference between IAP and WOA23 is
250 the smallest and Jingwei shows the strongest differences from IAP and other products. For 0-
251 2000 m, the depth average makes the difference between datasets much smaller. Jingwei still
252 shows relatively large discrepancy from the other datasets in the regions around 60°N and
253 the equator. Within the latitude range 20°S - 50°S where all other data products show the best
254 agreement, Jingwei exhibits a significant deviation of $\sim 5 \mu\text{mol kg}^{-1}$ from the rest.

255 However, the zonal mean O_2 concentration for 0-100 m (**Fig. 3b**) shows a relatively
256 distinct pattern. The zonal mean O_2 decreases linearly with the decrease of latitude for all the
257 datasets, except that for the high latitude range 60°S - 80°S , the zonal mean O_2 profiles
258 maintain a relatively stable value and the estimations between different data products vary to
259 an extent of $\sim 20 \mu\text{mol kg}^{-1}$ (**Fig. 3d**), which illustrates the relatively higher uncertainty in the
260 data reconstruction in this high latitude range.

261



262

263 **Figure 3** Global zonal mean O₂ concentration and differences for 0-1000 m (a, c) and 0-100
264 m (b, d) (unit: μmol kg⁻¹)

265

266 3.3 Spatial pattern

267 The spatial distribution of the upper 1000 m mean O₂ and the difference between IAP
268 and six other datasets is shown in **Fig. 4a-m**. The dataset of Jingwei is not included because
269 the spatial maps are not currently available. The difference of the 0-1000 m mean O₂ is
270 mainly within the magnitude of ~15 μmol kg⁻¹, which shows significant local differences
271 even though their differences are relatively small when averaged globally (~3 μmol kg⁻¹, **Fig.**
272 **2**). The mean O₂ of the GOBAI dataset is generally lower than IAP for 0-1000m (**Fig. 4f**),
273 consistent with the conclusions from the previous comparisons. There are bigger differences
274 located in the regions such as the subpolar North Pacific, the Southern Ocean fronts and the
275 eastern Pacific regions close to OMZ boundaries, where the strong spatial O₂ gradient, makes
276 the reconstruction sensitive to the mapping process and data distribution (Ito et al. 2025).
277 GOBAI, SJTU and GLODAP show a negative difference (~-15 μmol kg⁻¹) compared to IAP
278 for the upper 1000 m mean O₂ in most of the north and equatorial Pacific Ocean, and
279 equatorial Atlantic Ocean. WOA23 and GOBAI show a similar pattern of difference in the
280 Indian and Pacific Oceans: more positive offsets in the eastern Pacific/Indian Oceans and
281 negative offsets in the western Pacific/Indian Oceans. For the two generations of WOA



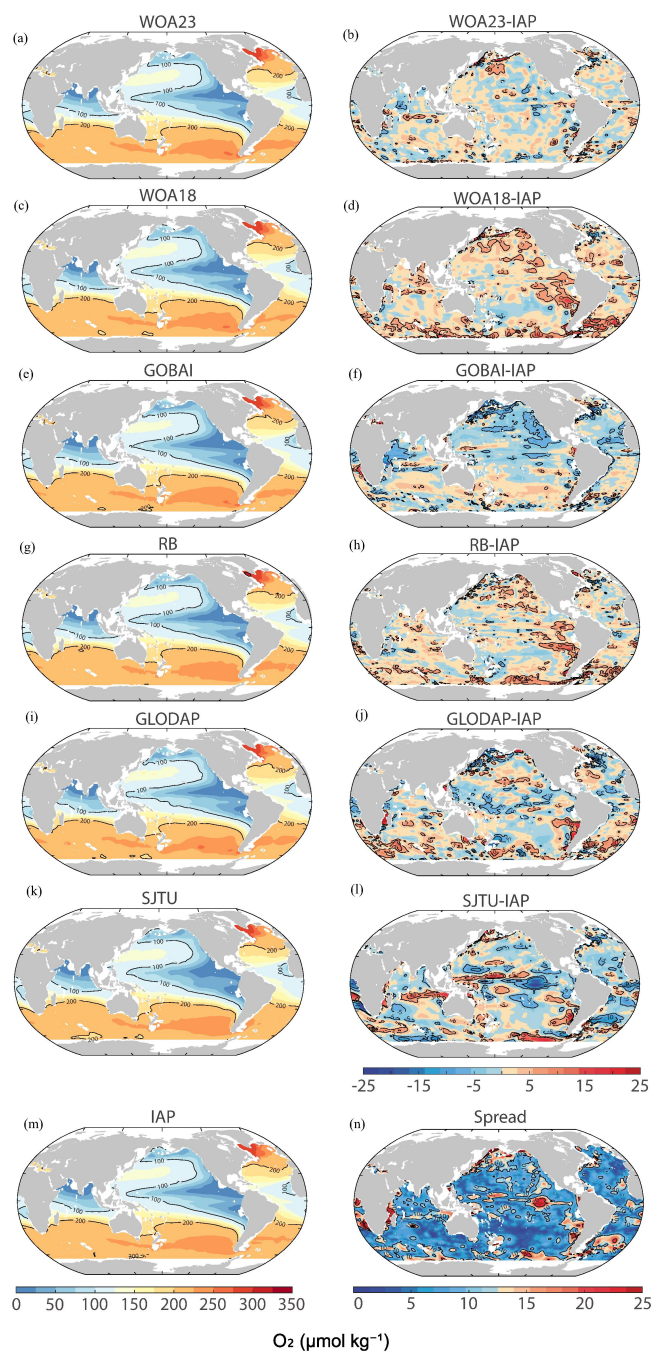
282 products, the difference between WOA23 and IAP is more negative globally than the
283 difference between WOA18 and IAP, likely due to the use of more recent data in WOA23.
284 SJTU exhibits a distinct pattern of differences, with substantial negative differences
285 occurring in the tropics.

286 The spatial map of the spread of the upper 1000 m mean climatological O₂ among all the
287 datasets except Jingwei is presented in **Fig. 4n**. The spread here is defined as the maximum
288 absolute value of the differences between all the other products and IAP. The spread is within
289 12 μmol kg⁻¹ in most of the ocean areas, with the largest spread reaching 25 μmol kg⁻¹ where
290 strong spatial O₂ gradients exist. The spread is generally lower in the Southern Hemisphere
291 than in the Northern Hemisphere, in contrast to the fact that there are more observations in
292 the North. This might be related to three issues: 1) A common error in the mapping method,
293 where the spatial interpolation generates over-smoothed or similar-biased fields in the
294 Southern Hemisphere; 2) the variability is lower in the Southern Hemisphere than in the
295 Northern Hemisphere, which reduces the reconstruction errors in the Southern Hemisphere; 3)
296 the deoxygenation trends are higher in the Northern Hemisphere than in the Southern thus the
297 spread reveals the O₂ level at different periods.

298 The exact reason can be explored with single-factor reconstruction experiments such as
299 Ito et al. (2025), which use the same input data but different mapping methods to isolate the
300 impact of mapping on climatology reconstruction. Further analyses are required, but it is
301 useful to know the differences between the products. When comparing the depth-mean O₂
302 between the eight datasets we adopted here which didn't distinguish different impact factors
303 in the process of generating gridded data products and aimed to illustrate a comprehensive
304 discrepancy, the difference for all the datasets for 0-300 m is within ±25 μmol kg⁻¹ and the
305 spread is up to 35 μmol kg⁻¹ (**Fig. S3**). The regions of high variability mainly locate in the
306 tropical and East Pacific, subpolar North Pacific and Southern Ocean fronts where there are
307 strong spatial O₂ gradient. However, when using the same quality-controlled observational
308 data as input and constraining the impact on data reconstruction to only the mapping method,
309 the difference of the mapped O₂ concentration between different mapping methods is within
310 ±10 μmol kg⁻¹ for 0-300 m (Ito et al., 2025). The overall difference between the data products
311 is more than two times of the difference constrained to a single factor of the mapping method,
312 indicating that the other factors, such as the quality controlled technique, bias correction,
313 vertical interpolation and so on, also contribute to the error source to a large extent. Further
314 analyses are required to assess and quantify the impact of every individual procedure on the



315 whole process of O₂ data reconstruction, but it is useful to know the differences between the
316 data products as a start.
317



318



319 **Figure 4** The spatial patterns of the upper 1000 m climatological mean O₂ concentration
320 (unit: $\mu\text{mol kg}^{-1}$). (a) WOA23, (b) WOA23-IAP, (c) WOA18, (d) WOA18-IAP, (e) GOBAl,
321 (f) GOBAl-IAP, (g) RB, (h) RB-IAP, (i) GLODAP, (j) GLODAP-IAP, (k) SJTU, (l) SJTU-
322 IAP, (m) IAP, (n) Spread is calculated as the difference of the upper 1000 m climatological
323 mean O₂ among the datasets.

324

325 3.4 Annual cycle

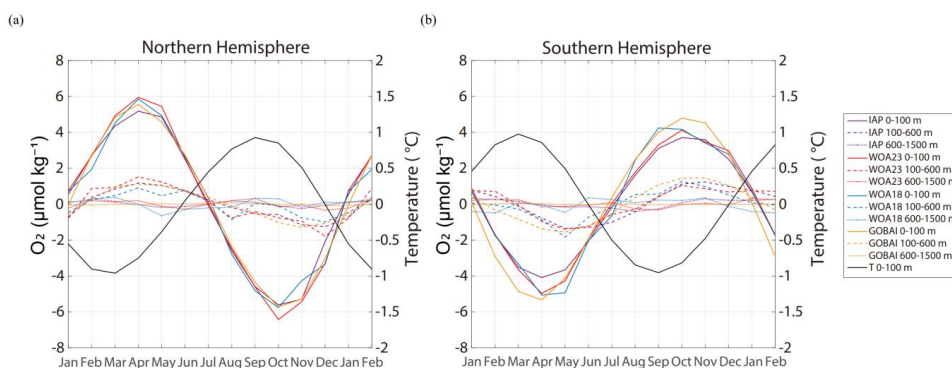
326 The annual cycle of the four products that provide a monthly climatology (IAP,
327 WOA23, WOA18 and GOBAl) is presented in **Fig. 5** for the 0-100 m, 100-600 m, and 600-
328 1500 m, and for northern and southern hemispheres, respectively calculated by the monthly
329 anomalies derived by subtracting the annual mean climatology of every data product
330 respectively. The annual cycle of the 0-100 m temperature for northern and southern
331 hemispheres is also calculated using the gridded temperature climatology product of IAP
332 (Cheng, et al., 2024). The magnitude of the O₂ seasonal cycle, defined as the maximum
333 amplitude of the annual variation, is greatest near the surface and decreases with depth.
334 Specifically, it is approximately $6 \mu\text{mol kg}^{-1}$ for the 0-100 m layer and $2 \mu\text{mol kg}^{-1}$ for the
335 deeper layer (100-600 m). The reduced annual cycle with depth is associated with stronger
336 annual variations of ocean temperature, wind-driven ventilation and biological processes in
337 the upper ocean compared to the deep ocean.

338 The appearance time of maximum (Apr.) and minimum (Oct.) O₂ levels in the northern
339 hemisphere are consistent among the four datasets for 0-100 m global mean O₂. Moreover,
340 the O₂ maximum in the depth layer in the northern and southern hemispheres for 0-100 m
341 lags about one month behind the temperature change, reflecting that besides the dominant
342 thermal induced increase in O₂ solubility, some physical/biological processes also impact the
343 concentration of ocean O₂ (Garcia et al., 2005; Wang et al., 2022). For the northern
344 hemisphere, the annual variation of the subsurface 100-600m layer also shows a pattern of
345 annual cycle with the maximum (Apr.) and minimum (Dec.) similar to the surface 0-100 m
346 layer, indicating that the O₂ annual cycle could penetrate to the deeper layer of ~600 m. It's
347 primarily due to the mechanisms including climatological winter mixed layer deepening,
348 which ventilates the subsurface, and seasonal thermocline dynamics coupled with organic
349 matter remineralization (Stamma et al., 2010). For the southern hemisphere, similar patterns
350 also exist.

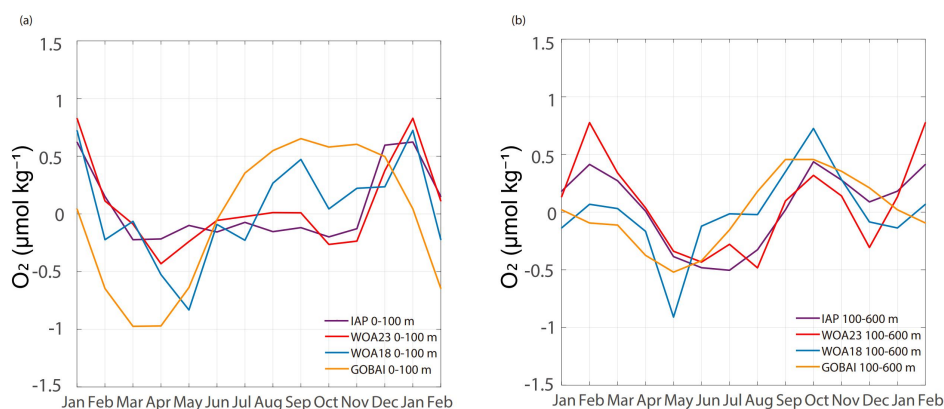
351 Although the two hemispheric O₂ annual cycles can be well-defined, the global mean is
352 more subtle, as different products show large differences in patterns of the global mean



353 annual cycle (**Fig. 6**). It appears that global 100-600 m O₂ annual cycles are more consistent
 354 across data products than 0-100 m, probably associated with noisier data and more natural
 355 variability near the sea surface. For global 100-600 m O₂, all datasets suggest an O₂ reduction
 356 from March to September and an increase from October to February, consistent with the
 357 Southern Hemisphere changes (**Fig. 6b** versus **Fig. 5b**). The magnitude of the global 0-100 m
 358 and 100-600 m annual cycle ranges from -1~0.8 μmol kg⁻¹ for the four datasets, but the
 359 standard deviation among the four datasets is ~0.3 μmol kg⁻¹ (~0.2 μmol kg⁻¹), indicating a
 360 similar level of signal and noise (**Fig. 6**).
 361



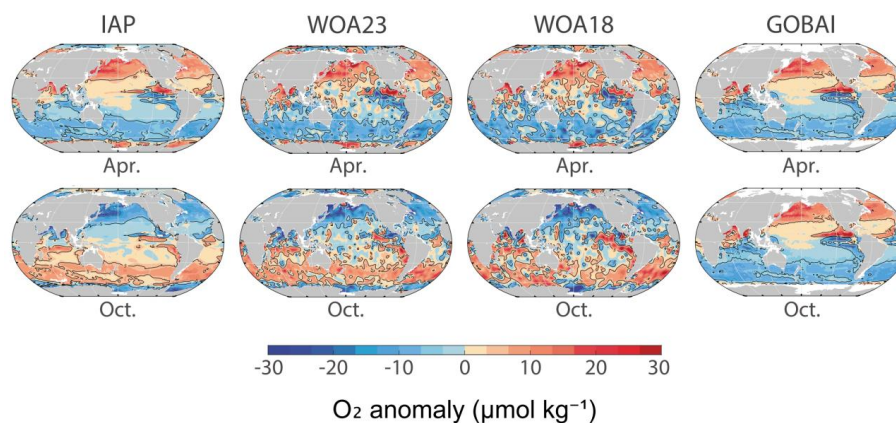
362
 363 **Figure 5** Annual variation of the (a) Northern Hemisphere and (b) Southern Hemisphere
 364 global mean O₂ for IAP, WOA23, WOA18 and GOBAI datasets.
 365



366
 367 **Figure 6** Global annual variation of the (a) 0-100 m and (b) 100-600 m global mean O₂ for
 368 IAP, WOA23, WOA18 and GOBAI datasets
 369



370 The annual cycle of O₂ anomalies shows a distinct spatial pattern (0-100 m mean O₂,
371 April versus October, **Fig. 7**). The anomalies are calculated by subtracting the annual mean
372 from the monthly climatologies for the four datasets (IAP, WOA23, WOA18, and GOBAI)
373 respectively. In April, the O₂ anomalies of 0-100 m in most of the northern hemisphere are
374 positive, and they turn negative in October. The tropical ocean annual cycle is not easily
375 defined, as many regions have semi-annual variability. Different products exhibit a consistent
376 pattern of change, whereas the detailed structures are quite distinct. In general, WOA23 and
377 WOA18 have more patchy characteristics than IAP and GOBAI, likely related to the
378 mapping methods employed by each: WOA uses an anti-distance weighted function to
379 interpolate the field; on the other hand, IAP uses model simulations to provide covariance
380 and GOBAI takes advantage of correlations between O₂ and temperature and salinity, both
381 building physical ocean properties into the reconstruction.
382



383

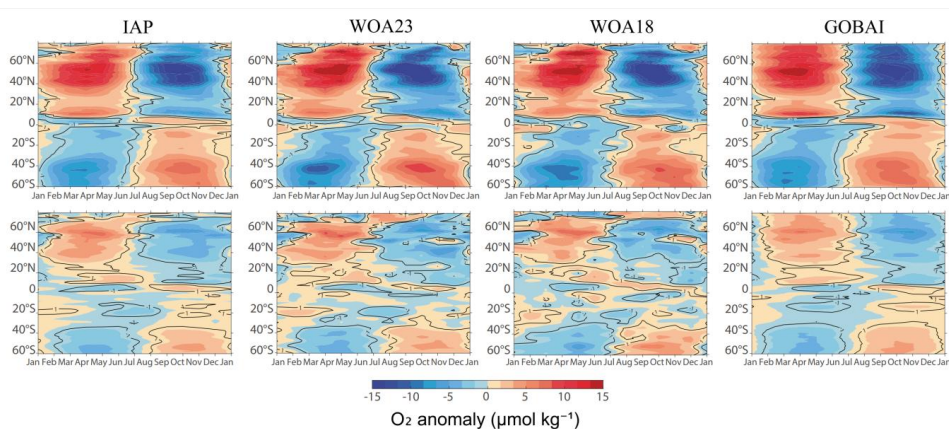
384 **Figure 7** Spatial distribution of the O₂ anomaly (0-100 m) for the IAP, WOA23, WOA18
385 and GOBAI climatology.

386

387 The zonal mean structure of the annual cycle is shown in **Fig. 8**, and all the datasets
388 show similar annual cycle patterns with some difference in smoothness and magnitude for
389 both 0-100 m and 100-600 m mean O₂. For 0-100 m, the largest seasonal changes occur in
390 the extra-tropics in the 30° to 60° belts of the northern hemisphere. In the southern
391 hemisphere, the largest seasonal changes occur in the latitudinal band centered near 40° S.
392 For both 0-100 m and 100-600 m, the phase transition occurs around July, which is consistent
393 for all datasets. Semi-annual cycles near the equator are visible in the upper ocean for almost



394 all products. There is a distinction of the annual cycle at about 10° N, corresponding to the
395 location of the intertropical convergence zone (ITCZ) (Garcia et al., 2005).
396



397
398 **Figure 8** Zonal mean annual cycles for 0-100 m (upper) and 100-600 m (lower) for different
399 data products.
400

401 To assess the patterns of annual cycle regionally, the zonal mean structures of the annual
402 cycle for different ocean basins are shown in **Fig. S4-S6**. Distinct seasonal changes exist in
403 the Pacific, Atlantic and Indian Ocean. The annual cycle patterns for the Pacific and Atlantic
404 Ocean coincide with the global O₂ annual cycle both for the 0-100 m and 100-600 m layers
405 closely. For the Indian Ocean, there are larger seasonal changes in the latitude range of ~10°-
406 20° N for 0-100 m than the Pacific and Atlantic Ocean. The annual variations of the mean O₂
407 for three major ocean basins (Pacific, Atlantic, Indian) for 0-100 m and 100-600 m are shown
408 in **Fig. S7-S9**, and also for the North and South Pacific/Atlantic respectively in **Fig. S10-S11**.
409 The magnitude of the O₂ seasonal cycle is greatest in the Atlantic Ocean (~3 μmol kg⁻¹) for
410 the 0-100 m layer, which corresponds to a magnitude of ~6 μmol kg⁻¹ in the North Atlantic
411 and ~4 μmol kg⁻¹ in the South Atlantic. The minimum and maximum O₂ levels (-4/6 μmol kg⁻¹)
412 and also occurrence time (Jul./Oct.) of WOA18 for 0-100 m differ the most from those of
413 the other three datasets in the South Atlantic (**Fig. S11b**).

414

415 3.5 Oxygen minimum zones

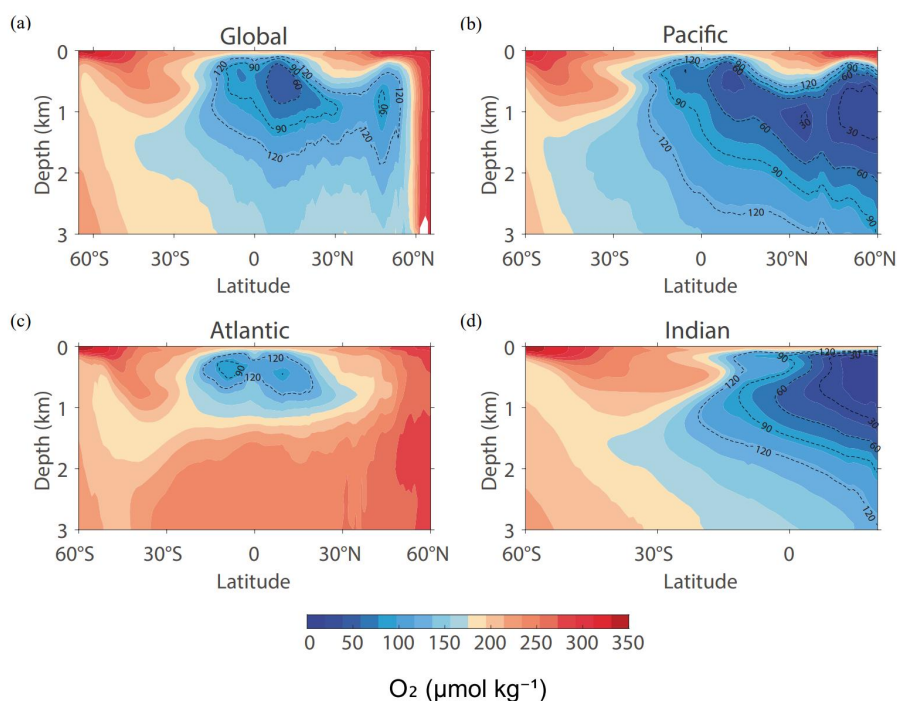
416 Oxygen minimum zones (OMZ) are important regions that impact marine organism
417 distributions and biogeochemical cycling. OMZ occur in various regions such as the tropical
418 Pacific and Atlantic Oceans, the North Pacific, and the North Indian Ocean, posing



419 challenges for marine organisms adapted to higher O_2 concentrations (Strammer et al., 2021).
420 In various studies, OMZ are bounded by different thresholds of O_2 levels. Here, we select
421 thresholds of $60 \mu\text{mol kg}^{-1}$ and $90 \mu\text{mol kg}^{-1}$ to define OMZ, referred to as OMZ60 and
422 OMZ90, respectively.

423 The zonal mean O_2 of the IAP climatology dataset for global and three major basins are
424 shown in **Fig. 9**. Globally, the zonal mean OMZ90 regions are mainly located within 200-
425 1200 m and 5°S - 30°N , associated with upwelling and high O_2 consumption. The Pacific
426 Ocean contains the largest volume of OMZ60 and OMZ90 among the three ocean basins,
427 with the OMZ90 extending from $\sim 15^\circ \text{S}$ to $\sim 60^\circ \text{N}$ and from a depth of ~ 200 m to ~ 3000 m.
428 There is a gradual increase in the max depth of OMZ90 and OMZ60 in the Pacific Ocean
429 from $\sim 15^\circ \text{S}$ to $\sim 60^\circ \text{N}$; thus, the OMZ in the North Pacific Ocean has greater vertical extent.
430 The OMZ in the North Pacific is also more severe because there is a notable region with
431 zonal O_2 levels less than $30 \mu\text{mol kg}^{-1}$ in the ~ 700 to ~ 1500 m layer. The OMZ90 in the
432 Indian Ocean extends from $\sim 10^\circ \text{S}$ to the northernmost end and is located from ~ 20 down to a
433 maximum depth of 1800 m. In the Atlantic Ocean, the OMZ90 is located within a 300-500 m
434 layer, with an area much smaller than that of the Pacific and Indian Oceans (**Table 2**).

435



436



437 **Figure 9** Comparison of zonal mean O₂ climatology (IAP climatology, unit: $\mu\text{mol kg}^{-1}$) in the
 438 (a) Global Ocean, (b) Pacific, (c) Atlantic, and (d) Indian oceans.

439

440 We also calculated the volume of OMZ60 and OMZ90 globally and for each basin in
 441 **Table 2** using six datasets, (excluding GOBAI and SJTU because their maximum depth only
 442 reaches about 2000 m below the ocean surface). The global volume of OMZ60 and OMZ90
 443 is generally consistent among the datasets, with a standard deviation of 1.95 % and 1.72 %
 444 across the products for OMZ60 and OMZ90, respectively. The Pacific Ocean contains most
 445 of the OMZ (83.05 % of the global OMZ60 and 81.29 % of the global OMZ90), with a
 446 standard deviation of 3.93 % and 2.37 % across the products. The Atlantic Ocean contains
 447 about 1.04 % and 2.38 % of the global OMZ60 and OMZ90, respectively, which is the lowest
 448 among the three ocean basins. The standard deviation is 20.24 % and 10.77 % for the Atlantic
 449 Ocean OMZ60 and OMZ90, respectively. The estimated OMZ for the Atlantic Ocean may be
 450 more sensitive to the horizontal resolution, mapping method and so on.

451

452 **Table 2** The volume of OMZ60 and OMZ90 calculated from the annual mean climatology
 453 for each basin and for different products. The values are in the units of 10^6 km^3 .

	OMZ60				OMZ90			
Datasets	Global	Pacific	Atlantic	Indian	Global	Pacific	Atlantic	Indian
IAP	81.76	68.98	0.85	11.91	152.78	125.56	3.83	23.36
WOA23	83.79	69.90	0.88	12.49	155.46	126.86	3.72	24.33
WOA18	79.42	66.71	0.74	11.46	152.23	124.93	3.50	23.28
RB	80.93	67.73	0.94	11.74	152.69	124.95	3.93	23.26
GLODAP	80.68	68.18	1.07	11.42	146.69	119.85	3.93	22.90
Jingwei	78.99	61.74	0.52	12.63	152.14	119.19	2.81	23.70
Mean	80.92	67.21	0.84	11.94	152.00	123.56	3.62	23.47
Standard Deviation	1.58	2.64	0.17	0.47	2.62	2.93	0.39	0.45

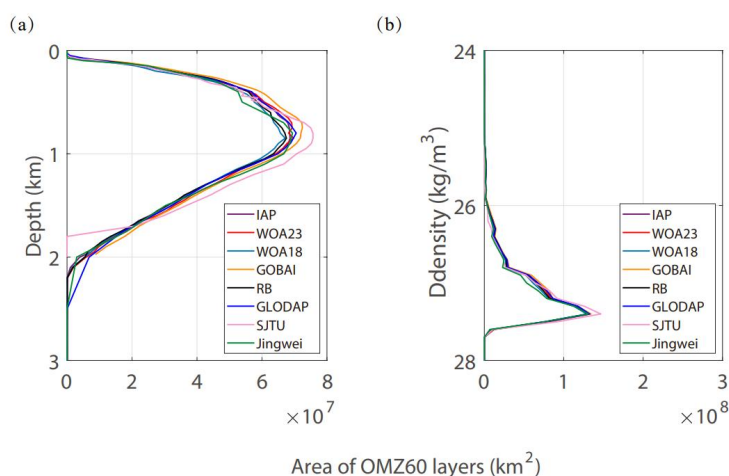
454



455

456 The OMZ areas as a function of depth and density are shown in **Fig. 10**. The density
457 layers are calculated with the Gibbs-SeaWater (GSW) Oceanographic Toolbox (IOC et al.,
458 2010; McDougall & Barker, 2011; Kwiecinski and Babbin, 2021), using the gridded
459 temperature and salinity climatology products of IAP (Cheng, et al., 2024). The maximum
460 OMZ60 area occurs at a depth of ~ 800 m and a density of 27.75 kg m^{-3} for all the datasets.
461 Most OMZ60s exist in the upper 2000 m. GOBAI and SJTU exhibit a larger OMZ60 volume
462 within the upper 2000 m compared to other products, and the maximum depth of SJTU
463 OMZ60 is ~ 1700 m, which is shallower than that of the other products. At density levels, the
464 products are very consistent, and SJTU shows a larger area of OMZ60 near the 27.4 kg m^{-3}
465 level and Jingwei shows a smaller area of OMZ60 near the 27 kg m^{-3} level.

466



467

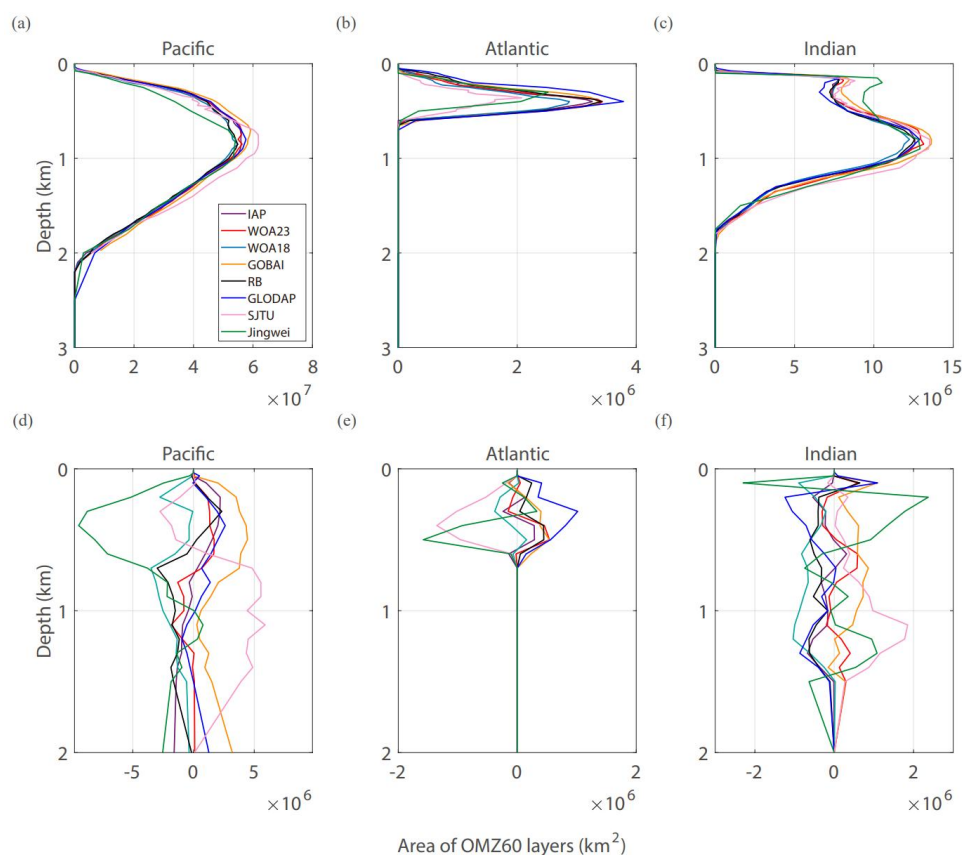
468 **Figure 10** The global horizontal area of OMZ60 in each interpolated layer with respect to
469 (a) depth and (b) density.

470

471 **Figure 11a-c** shows the horizontal OMZ60 area at depth levels for the Pacific, Atlantic,
472 and Indian Ocean basins, respectively. Consistent with the volume assessment in Table 2, the
473 Pacific Ocean contains the largest OMZ60 area, followed by the Indian and Atlantic Oceans.
474 The maximum OMZ60 area occurs at a depth of about 800m in the Pacific and Indian
475 Oceans, but at a much shallower depth of ~ 400 m in the Atlantic Ocean. Jingwei shows the
476 largest difference from the other products in the Pacific and Indian Oceans at the upper 500
477 m depth. SJTU shows a larger area of OMZ60 in the Pacific and Indian Oceans but a smaller



478 area in the Atlantic Ocean than the other products (**Fig. 11**). Collectively, different products
479 show a spread of $\pm 4 \times 10^6 \text{ km}^2$ for the Pacific OMZ60, $\pm 1 \times 10^6 \text{ km}^2$ for the Indian and
480 Atlantic OMZ60 (**Fig. 11d-f**), except that Jingwei shows a very large difference of up to -9
481 $\times 10^6 \text{ km}^2$ at the depth around 500m for the Pacific OMZ60 area compared to the ensemble
482 mean (**Fig. 11d**).



483

484 **Figure 11** OMZ60 area for the Pacific, Atlantic, and Indian Ocean basins in units of 10^6 km^2 .

485 The upper row is the vertical distribution of the OMZ areas: (a) Pacific, (b) Atlantic, (c)
486 Indian. The lower row is the differences in the OMZ areas relative to the ensemble mean: (d)
487 Pacific, (e) Atlantic, (f) Indian.

488

489 **4 Conclusion**

490 Observationally-based gridded data products provide a basis for detecting and
491 understanding ocean O_2 changes at various spatial and temporal scales. These observational
492 datasets are also used to validate the computational ocean biogeochemistry and earth system



493 models. This study provides a quantitative description of the O₂ climatology, annual cycle
494 and OMZ distribution with eight O₂ data products. There have been several new O₂ data
495 products developed in recent years, which makes this comparative analysis timely.

496 The global mean O₂ shows a well-established high-low-high vertical structure and a
497 good consistency among all products. The global mean O₂ concentrations of the products
498 over depth generally agree within $\pm 3 \mu\text{mol kg}^{-1}$. Regionally, the gridded mean difference of
499 the 0-1000 m mean O₂ is mainly within $\sim 12 \mu\text{mol kg}^{-1}$. For the global 0-100 m O₂ annual
500 cycle, O₂ anomalies (differences from the annual mean) ranges from -1 to $0.8 \mu\text{mol kg}^{-1}$, but
501 the inter-products difference (defined by the standard deviation of four datasets that provide a
502 monthly climatology) can be as large as $\sim 0.3 \mu\text{mol kg}^{-1}$, indicating a similar signal-to-noise
503 ratio among the four datasets of monthly climatology. We also analyze the OMZ distribution
504 for different climatology datasets. Different products show a spread of $\pm 4 \times 10^6 \text{ km}^2$ for the
505 Pacific OMZ60 and $\pm 1 \times 10^6 \text{ km}^2$ for the Indian and Atlantic OMZ60.

506 The assessments presented in this study demonstrate the consistency and differences
507 among available products, supporting their future use. Significant local differences ($\pm 25 \mu$
508 mol kg^{-1} for the upper 1000 m climatological mean) could be observed when we assess the
509 climatologies by its depth-mean spatial distribution. This level of uncertainty could influence
510 the baseline from which anomalies and trends are calculated and could give an insight into
511 regions where the accuracy of gridded data reconstruction is relatively more sensitive to the
512 mapping method and observation data distribution, such as the subpolar North Pacific, the
513 Southern Ocean fronts and the eastern Pacific regions close to OMZ boundaries where the
514 spatial O₂ gradient is large. Quantifying these discrepancies could enable the prioritization of
515 observation instrument deployments and further advance the improvement of gridded O₂ data
516 reconstruction processes.

517 Because the overall uncertainties resulting from a combined effect of all uncertainty
518 sources (e.g., measurements, mapping error, different time periods, etc.) for the ocean O₂
519 climatology datasets are measured here, this study provides a basis for further studies that
520 may attempt to understand the contribution of a single factor. For example, the Gridded
521 Observational Dataset Intercomparison Project-Dissolved Oxygen (GODIP-DO) aims to
522 isolate each error source, such as mapping and quality control, based on the same input data
523 for a smaller number of datasets. Thus, comparing the results of this study with their
524 outcomes will provide insight into the key contributions of the difference between products.
525 Such insights will eventually help the community to improve the methodologies and reduce



526 the spread in the future. Another caveat is that only limited number of products are included
527 in this inter-comparison, we hope to maintain and extend this activity in the future and serve
528 as a regular practice to provide critical information to the data users.

529

530 **Data availability**

531 All the gridded data products used in this study are available at:

532 GODIP-DO Group: Global Dissolved Oxygen Gridded Climatological Datasets, Zenodo[data
533 set], <https://doi.org/10.5281/zenodo.16664650>. 2025.

534

535 **Author contributions**

536 JD and LC-conceptualization, supervision, methodology; JD-formal analysis, visualization,
537 writing; JD, LC, HEG, ZW, JDS, CJR, YZ and BL-data curation; TI, HEG, ZW, JDS, GGN,
538 SMB and SM-writing.

539

540 **Competing interests**

541 The contact author has declared that none of the authors has any competing interests.

542

543 **Financial support**

544 IAP authors gratefully acknowledge support by National Natural Science Foundation of
545 China (grant no. 42261134536), the new Cornerstone Science Foundation through the
546 XPLOER PRIZE and the Asian Cooperation Fund, and the International Partnership
547 Program of the Chinese Academy of Sciences (Grant No. 060GJHZ2024064MI). TI and JDS
548 are supported by funding from the US National Science Foundation (OCE-2446011,
549 2446012). This is CICOES contribution no. 2025-1474 and PMEL contribution no. 5797.

550

551 **References**

552 Bindoff, N. L., Cheung, W. W. L., Kairo, J. G., Aristegui, J., Guinder, V. A., Hallberg, R.,
553 Hilmi, N., Jiao, N., Karim, M. S., Levin, L., O'Donoghue, S., Purca Cuicapusa, S. R.,
554 Rinkevich, B., Suga, T., Tagliabue, A., and Williamson, P.: Changing Ocean, marine
555 ecosystems, and dependent communities, In: IPCC Special Report on the Ocean and
556 Cryosphere in a Changing Climate, Cambridge University Press, Cambridge, UK and
557 New York, NY, USA, 447-587, <https://doi.org/10.1017/9781009157964.007>, 2019.

558

559 Boyer, T. P., Baranova, O. K., Coleman, C., Garcia, H. E., Grodsky, A., Locarnini, R. A.,
560 Mishonov, A. V., Paver, C. R., Reagan, J. R., Seidov, D., Smolyar, I. V., Weathers, K.,
561 and Zweng, M. M.: World Ocean Database 2018, Mishonov, A. V., Technical Editor,
562 NOAA Atlas NESDIS 87, 2018.



- 563
564 Breitburg, D., Levin, L. A., Oschlies, A., Grégoire, M., Chavez, F. P., Conley, D. J., Garçon,
565 V., Gilbert, D., Gutiérrez, D., Isensee, K., Jacinto, G. S., Limburg, K. E., Montes, I.,
566 Naqvi, S. W. A., Pitcher, G. C., Rabalais, N. N., Roman, M. R., Rose, K. A., Seibel, B.
567 A., Telszewski, M., Yasuhara, M., and Zhang, J.: Declining oxygen in the global ocean
568 and coastal waters, *Science*, 359, eaam7240, <https://doi.org/10.1126/science.aam7240>,
569 2018.
- 570
571 Cheng, L. and Zhu, J.: Benefits of CMIP5 Multimodel Ensemble in Reconstructing Historical
572 Ocean Subsurface Temperature Variations, *J. Clim.*, 29, 5393-5416,
573 <https://doi.org/10.1175/JCLI-D-15-0730.1>, 2016.
- 574
575 Cheng, L., Trenberth, K. E., Fasullo, J., Boyer, T., Abraham, J., and Zhu, J.: Improved
576 estimates of ocean heat content from 1960 to 2015, *Sci. Adv.*, 3, e1601545,
577 <https://doi.org/10.1126/sciadv.1601545>, 2017.
- 578
579 Cheng, L., Pan, Y., Tan, Z., Zheng, H., Zhu, Y., Wei, W., Du, J., Yuan, H., Li, G., Ye, H.,
580 Gouretski, V., Li, Y., Trenberth, K. E., Abraham, J., Jin, Y., Reseghetti, F., Lin, X.,
581 Zhang, B., Chen, G., Mann, M. E., and Zhu, J.: IAPv4 ocean temperature and ocean heat
582 content gridded dataset, *Earth Syst. Sci. Data*, 16, 3517-3546,
583 <https://doi.org/10.5194/essd-16-3517-2024>, 2024.
- 584
585 Deutsch, C., Brix, H., Ito, T., Frenzel, H., and Thompson, L.: Climate-forced variability of
586 ocean hypoxia, *Science*, 333, 336-339, <https://doi.org/10.1126/science.1202422>, 2011.
- 587
588 Garcia, H. E., Boyer, T. P., Levitus, S., Locarnini, R. A., and Antonov, J.: On the variability
589 of dissolved oxygen and apparent oxygen utilization content for the upper world ocean:
590 1955 to 1998, *Geophys. Res. Lett.*, 32, L09604, <https://doi.org/10.1029/2004GL022286>,
591 2005.
- 592
593 Garcia, H. E., Boyer, T. P., Levitus, S., Locarnini, R. A., and Antonov, J.: Climatological
594 annual cycle of upper ocean oxygen content anomaly, *Geophys. Res. Lett.*, 32, L05611,
595 <https://doi.org/10.1029/2004GL021745>, 2005.
- 596
597 Garcia, H. E., Weathers, K., Paver, C. R., Smolyar, I., Boyer, T. P., Locarnini, R. A., Zweng,
598 M. M., Mishonov, A. V., Baranova, O. K., Seidov, D., and Reagan, J. R.: World Ocean
599 Atlas 2018, Volume 3: Dissolved Oxygen, Apparent Oxygen Utilization, and Oxygen
600 Saturation, A. Mishonov Technical Ed., NOAA Atlas NESDIS 83, 2018.
- 601
602 Garcia, H. E., Wang, Z., Bouchard, C., Cross, S. L., Paver, C. R., Reagan, J. R., Boyer, T. P.,
603 Locarnini, R. A., Mishonov, A. V., Baranova, O. K., Seidov, D., and Dukhovskoy, D.:
604 World Ocean Atlas 2023, Volume 3: Dissolved Oxygen, Apparent Oxygen Utilization,
605 Dissolved Oxygen Saturation, and 30-year Climate Normal, A. Mishonov Technical
606 Editor, NOAA Atlas NESDIS 91, 100 pp., <https://doi.org/10.25923/rb67-ns53>, 2024.
- 607
608 Garcia-Soto, C., Cheng, L., Caesar, L., Schmidtko, S., Jewett, E. B., Cheripka, A., Rigor, I.,
609 Caballero, A., Chiba, S., Báez, J. C., Zielinski, T., and Abraham, J. P.: An Overview of
610 Ocean Climate Change Indicators: Sea Surface Temperature, Ocean Heat Content,
611 Ocean pH, Dissolved Oxygen Concentration, Arctic Sea Ice Extent, Thickness and
612 Volume, Sea Level and Strength of the AMOC (Atlantic Meridional Overturning



- 613 Circulation), *Front. Mar. Sci.*, 8, 642372, <https://doi.org/10.3389/fmars.2021.642372>,
614 2021.
615
616 Gouretski, V., Cheng, L., Du, J., Xing, X., and Chai, F.: A quality-controlled and bias-
617 adjusted global ocean oxygen profile dataset, Marine Science Data Center of the Chinese
618 Academy of Sciences, <http://dx.doi.org/10.12157/IOCAS.20231208.001>, 2024.
619
620 Gouretski, V., Cheng, L., Du, J., Xing, X., Chai, F., and Tan, Z.: A consistent ocean oxygen
621 profile dataset with new quality control and bias assessment, *Earth Syst. Sci. Data*, 16,
622 5503-5530, <https://doi.org/10.5194/essd-16-5503-2024>, 2024.
623
624 Gregoire, M., Garçon, V., Garcia, H., Oeschies, A., Schmidtko, S., Isensee, K., et al.: A
625 Global Ocean Oxygen Database and Atlas for Assessing and Predicting Deoxygenation
626 and Ocean Health in the Open and Coastal Ocean, *Front. Mar. Sci.*, 8, 1-29,
627 <https://doi.org/10.3389/fmars.2021.724913>, 2021.
628
629 Gulev, S. K., Thorne, P. W., Ahn, J., Dentener, F. J., Domingues, C. M., Gerland, S., Gong,
630 D., Kaufman, D. S., Nnamchi, H. C., Quaas, J., Rivera, J. A., Sathyendranath, S. L.,
631 Smith, S. L., Trewin, B., von Schuckmann, K., and Vose, R. S.: Changing State of the
632 Climate System, In: *Climate Change 2021: The Physical Science Basis. Contribution of*
633 *Working Group I to the Sixth Assessment Report of the Intergovernmental Panel on*
634 *Climate Change*, edited by: Masson-Delmotte, V., Zhai, P., Pirani, A., Connors, S. L.,
635 Péan, C., Berger, S., Caud, N., Chen, Y., Goldfarb, L., Gomis, M. I., Huang, M., Leitzell,
636 K., Lonnoy, E., Matthews, J. B. R., Maycock, T. K., Waterfield, T., Yelekçi, O., Yu, R.,
637 and Zhou, B., Cambridge University Press, Cambridge, United Kingdom and New York,
638 NY, USA, 287-422, <https://doi.org/10.1017/9781009157896.004>, 2021.
639
640 Huang, S., Shao, J., Chen, Y., Qi, J., Wu, S., Zhang, F., He, X., and Du, Z.: Reconstruction of
641 dissolved oxygen in the Indian Ocean from 1980 to 2019 based on machine learning
642 techniques, *Front. Mar. Sci.*, 10, 1291232, <https://doi.org/10.3389/fmars.2023.1291232>,
643 2023.
644
645 IOC, SCOR, and IAPSO: The International thermodynamic equation of seawater-2010:
646 Calculation and use of thermodynamic properties, Intergovernmental Oceanographic
647 Commission, Manuals and Guides No. 56, UNESCO, 2010.
648
649 Ito, T., Minobe, S., Long, M. C., and Deutsch, C.: Upper ocean O₂ trends: 1958-2015,
650 *Geophys. Res. Lett.*, 44, 4214-4223, <https://doi.org/10.1029/2017GL073613>, 2017.
651
652 Ito, T., Cervania, A., Cross, K., Ainchwar, S., and Delawalla, S.: Mapping dissolved oxygen
653 concentrations by combining shipboard and Argo observations using machine learning
654 algorithms, *J. Geophys. Res.-Mach. Learn. Comput.*, 1, e2024JH000272,
655 <https://doi.org/10.1029/2024JH000272>, 2024.
656
657 Ito, T., Garcia, H. E., Wang, Z., Cheng, L., Du, J., Roach, C. J., Sharp, J. D., Minobe, S.,
658 Zhou, Y., Lu, B., Navarra, G. G., and Bushinsky, S. M.: Assessing the observational
659 uncertainties of dissolved oxygen climatology and seasonal cycle through a coordinated
660 intercomparison project, *Global Biogeochem. Cy.*, 39, e2025GB008751,
661 <https://doi.org/10.1029/2025GB008751>, 2025.
662



- 663 Keeling, R. F., Körtzinger, A., and Gruber, N.: Ocean Deoxygenation in a Warming world,
664 *Annu. Rev. Mar. Sci.*, 2, 199-229,
665 <https://doi.org/10.1146/annurev.marine.010908.163855>, 2010.
666
- 667 Koelling, J., Atamanchuk, D., Karstensen, J., Handmann, P., and Wallace, D. W. R.: Oxygen
668 export to the deep ocean following Labrador Sea Water formation, *Biogeosciences*, 19,
669 437-454, <https://doi.org/10.5194/bg-19-437-2022>, 2022.
670
- 671 Kwiecinski, J. V., and Babbin, A. R.: A high-resolution atlas of the eastern tropical Pacific
672 oxygen deficient zones, *Global Biogeochem. Cy.*, 35, e2021GB007001,
673 <https://doi.org/10.1029/2021GB007001>, 2021.
674
- 675 Lauvset, S. K., Key, R. M., Olsen, A., van Heuven, S., Velo, A., Lin, X., Schirnick, C.,
676 Kozyr, A., Tanhua, T., Hoppema, M., Jutterström, S., Steinfeldt, R., Jeansson, E., Ishii,
677 M., Perez, F. F., Suzuki, T., and Watelet, S.: A new global interior ocean mapped
678 climatology: the $1^\circ \times 1^\circ$ GLODAP version 2, *Earth Syst. Sci. Data*, 8, 325-340,
679 <https://doi.org/10.5194/essd-8-325-2016>, 2016.
680
- 681 Levin, L. A.: Manifestation, drivers, and emergence of open ocean deoxygenation, *Annu.*
682 *Rev. Mar. Sci.*, 10, 229-260, <https://doi.org/10.1146/annurev-marine-121916-063359>,
683 2018.
684
- 685 Liu, Q. H., Bao, S. L., Yan, H. Q., Wang, H. Z., and Zhang, R.: Enhancing sea surface
686 salinity short-term prediction using physically informed deep learning, *Appl. Ocean*
687 *Res.*, 165, 104832, <https://doi.org/10.1016/j.apor.2025.104832>, 2025.
688
- 689 Lu, B., Zhao, Z., Han, L. Y., Gan, X. Y., Zhou, Y. T., Zhou, L., Fu, L. Y., Wang, X. B.,
690 Zhou, C. H., and Zhang, J.: A Spatio-Temporal Graph Hypernetwork for Reconstruction
691 of Global Ocean Dissolved Oxygen, *Proceedings of the 41st International Conference on*
692 *Machine Learning*, Vienna, Austria, PMLR 235, 2024.
693
- 694 McDougall, T. J., and Barker, P. M.: Getting started with TEOS-10 and the Gibbs Seawater
695 (GSW) oceanographic toolbox, *SCOR/IAPSO WG127*, 1-28, 2011.
696
- 697 Mishonov, A. V., Boyer, T. P., Baranova, O. K., Bouchard, C., Cross, S. L., Garcia, H. E.,
698 Locarnini, R. A., Paver, C. R., Reagan, J. R., Wang, Z., Seidov, D., Grodsky, A. I., and
699 Beauchamp, J. G.: *World Ocean Database 2023*, C. Bouchard, Technical Ed., NOAA
700 Atlas NESDIS 97, <https://doi.org/10.25923/z885-h264>, 2024.
701
- 702 Musan, I., Gildor, H., Barkan, E., Smethie, W. M., Jr., and Luz, B.: Evidence from dissolved
703 O₂ isotopes in North Atlantic Deep Water for a recent climatic shift, *Geophys. Res.*
704 *Let.*, 50, e2022GL100489, <https://doi.org/10.1029/2022GL100489>, 2023.
705
- 706 Oschlies, A., Duteil, O., Getzlaff, J., Koeve, W., Landolfi, A., and Schmidtko, S.: Patterns of
707 deoxygenation: sensitivity to natural and anthropogenic drivers, *Philos. T. R. Soc. A*,
708 375, 20160325, <https://doi.org/10.1098/rsta.2016.0325>, 2017.
709
- 710 Oschlies, A., Brandt, P., Stramma, L., and Schmidtko, S.: Drivers and mechanisms of ocean
711 deoxygenation, *Nat. Geosci.*, 11, 467-473, <https://doi.org/10.1038/s41561-018-0152-2>,
712 2018.



- 713
714 Roach, C. J., and Bindoff, N. L.: Developing a New Oxygen Atlas of the World's Oceans
715 Using Data Interpolating Variational Analysis, *J. Atmos. Ocean. Tech.*, 40, 1475-1491,
716 <https://doi.org/10.1175/JTECH-D-23-0007.1>, 2023.
717
- 718 Ruhl, H. A., Huffard, C. L., Messié, M., Connolly, T. P., Soltwedel, T., Wenzhöfer, F.,
719 Wallace, D. W. R., et al.: Decadal change in deep-ocean dissolved oxygen in the North
720 Atlantic Ocean and North Pacific Ocean, *Deep-Sea Res. Pt. I*, 223, 104534,
721 <https://doi.org/10.1016/j.dsr.2025.104534>, 2025.
722
- 723 Schmidtko, S., Stramma, L., and Visbeck, M.: Decline in global oceanic oxygen content
724 during the past five decades, *Nature*, 542, 335-339, <https://doi.org/10.1038/nature21399>,
725 2017.
726
- 727 Sharp, J. D., Fassbender, A. J., Carter, B. R., Johnson, G. C., Schultz, C., and Dunne, J. P.:
728 GOBAI-O2: temporally and spatially resolved fields of ocean interior dissolved oxygen
729 over nearly 2 decades, *Earth Syst. Sci. Data*, 15, 4481-4518,
730 <https://doi.org/10.5194/essd-15-4481-2023>, 2023.
731
- 732 Stramma, L., Johnson, G. C., Sprintall, J., and Mohrholz, V.: Expanding oxygen-minimum
733 zones in the tropical oceans, *Science*, 320, 655-658,
734 <https://doi.org/10.1126/science.1153847>, 2008.
735
- 736 Stramma, L., and Schmidtko, S.: Spatial and temporal variability of oceanic oxygen changes
737 and underlying trends, *Atmos.-Ocean*, 59, 122-132,
738 <https://doi.org/10.1080/07055900.2021.1905601>, 2021.
739
- 740 Wang, Z., Garcia, H. E., Boyer, T. P., Reagan, J., and Cebrian, J.: Controlling factors of the
741 climatological annual cycle of the surface mixed layer oxygen content: A global view,
742 *Front. Mar. Sci.*, 9, 1001095, <https://doi.org/10.3389/fmars.2022.1001095>, 2022.
743
- 744 Whitney, F. A., Bograd, S. J., and Ono, T.: Nutrient enrichment of the subarctic Pacific
745 Ocean pycnocline, *Geophys. Res. Lett.*, 40, 2200-2205,
746 <https://doi.org/10.1002/grl.50439>, 2013.
747
- 748 Zhou, Y., Gong, H., and Zhou, F.: Responses of horizontally expanding oceanic oxygen
749 minimum zones to climate change based on observations, *Geophys. Res. Lett.*, 49,
750 e2022GL097724, <https://doi.org/10.1029/2022GL097724>, 2022.
751
752